

# Data-Efficient Inference of Neural Fluid Fields via SciML Foundation Model

Yuqiu Liu<sup>1\*</sup>, Jingxuan Xu<sup>2\*</sup>, Mauricio Soroco<sup>1</sup>, Yunchao Wei<sup>2,3</sup>, Wuyang Chen<sup>1</sup>  
<sup>1</sup>Simon Fraser University <sup>2</sup>Beijing Jiaotong University <sup>3</sup>Peng Cheng Laboratory

## Abstract

Recent developments in 3D vision have enabled successful progress in inferring **neural fluid fields** and realistic rendering of fluid dynamics. However, these methods require real-world flow captures, which demand dense video sequences and specialized lab setups, making the process costly and challenging. Scientific machine learning (SciML) foundation models, which are pretrained on extensive simulations of partial differential equations (PDEs), encode rich multiphysics knowledge and thus provide promising sources of domain priors for inferring fluid fields. Nevertheless, their potential to advance real-world vision problems remains largely underexplored, raising questions about the transferability and practical utility of these foundation models. In this work, we demonstrate that SciML foundation model can significantly improve the **data efficiency** of inferring real-world 3D fluid dynamics with improved generalization. At the core of our method is leveraging the strong forecasting capabilities and meaningful representations of SciML foundation models. We equip neural fluid fields with a novel collaborative training approach that utilizes augmented views and fluid features extracted by our foundation model. Our method demonstrates significant improvements in both quantitative metrics and visual quality, showcasing the practical applicability of SciML foundation models in real-world fluid dynamics.

## 1. Introduction

Fluid phenomena are ubiquitous in our 3D world, from the powerful ocean currents shaping coastlines to the turbulent jet streams in the air. One important yet open challenge in understanding fluids is to recover fluid dynamics from visual observations, also known as the inference of **3D fluid fields**. Formally stated, given visual inputs (2D images or video sequences), this task aims to infer invisible quantities like density, velocity, vorticity, pressure, in the spatiotemporal domain (3+1D), as shown in Figure 1 left. This facilitates downstream rendering of realistic fluids in computer games and videos [69], and even applications of

broad impacts such as weather forecasting [49] and airfoil design [63]. Unlike rigid bodies, fluids present a unique challenge due to their dynamic and complex nature, requiring advanced computational methods.

Recent advancements in 3D computer vision have enabled significant progress in inferring fluid fields. This includes both multi-view benchmarks [16] of high-quality flow videos with well-calibrated camera poses, and also neural fluid fields [10–12, 23, 80] jointly optimized by rendering loss and physics constraints. However, learning to infer fluid fields with deep networks is notorious for its **heavy data consumption** of densely captured fluid views. Methods like HyFluid [80] by default require four videos with 120 continuous frames each. This requirement is often expensive and impractical, relying on specialized lab setups such as lasers or particle tracking. For example, collecting and calibrating the ScalarFlow dataset [16] requires insulated containers with heaters, fog machines with servo-controlled valves, and multiple cameras, with an estimated total cost of around \$1,100.

A common strategy to achieve data efficiency and improved generalization is to introduce appropriate prior knowledge. Scientific machine learning (SciML), which aims to learn physical dynamics, is a promising source of prior knowledge to introduce (Figure 1 right). Deep neural networks (DNNs) provide surrogate models for rapid approximations of partial differential equations (PDEs) and

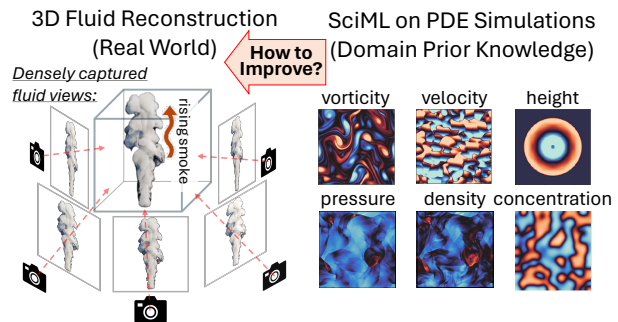


Figure 1. Inferring neural fluid fields requires densely captured views. Meanwhile, PDE simulations are important for building SciML foundation models. How to utilize this rich domain knowledge and improve 3D fluid reconstruction in the real world?

\*The first two authors contributed equally.

real-world challenges like weather forecasting [38, 49] and turbulent flow [31]. **SciML foundation models** are further advanced in recent works [25, 26, 43, 51, 58, 60, 68, 79]. By scaling up extensive training datasets to incorporate multiple physical domains and PDE simulations, SciML foundation models aim to encode common physical behaviors and enhance generalization and scalability within scientific contexts, such as dynamics of fluid, smoke, and airflow.

Although promising, SciML foundation models are mainly pretrained and evaluated on PDE simulations [45, 59, 61], especially for fluid dynamics (Navier-Stokes, Burgers’, shallow water). These simulations, while encoding rich physical domain knowledge, still differ from real fluid captures with multiscale phenomena, noisy measurements, and changing environments (Figure 1). This poses questions about the transferability and utility of SciML foundation models in real-world 3D fluid problems. In contrast, foundation models in popular ML domains have been widely utilized as strong prior knowledge. Vision models such as DiNO [5, 48] and CLIP [50] have been extensively leveraged to extract meaningful and generalizable representations and also semantic awareness [6, 42, 62, 66, 71, 73, 78]. Large language models (LLMs), such as GPT [1] and Llama [15, 64, 65], are pretrained on high-quality corpora and interact with the informal spoken language of human users every day. Therefore, we ask our core question:

*How to utilize SciML foundation models to advance 3D reconstruction of real-world fluids?*

In this work, we provide affirmative answers (Figure 2), and demonstrate that pretrained SciML foundation models can enhance data efficiency in inferring neural fluid fields from sparse videos (estimating fluid density and velocity from videos). Our core idea is to utilize the multi-physics domain knowledge encoded in our SciML foundation model, and leverage its strong forecasting and meaningful representations to “distill” this prior into neural fluid fields. We demonstrate both improved quantitative metrics and the high-quality visual appearance of our method on real-world flow captures with significantly reduced training input views. We summarize our contributions below:

1. Given extremely sparse initial views from short videos of flows, we utilize our foundation model to forecast future steps (temporal frames)<sup>1</sup>, which leads to a collaborative training strategy for neural fluid fields with more augmented fluid views (Section 3.2 and Figure 6).
2. To improve generalization, we introduce meaningful representations of flows extracted by our foundation model into neural fluid fields, by carefully aligning the representation with camera rays used to infer the fluid field (Section 3.3 and Figure 7).

<sup>1</sup>In this work, we use “frame” and “view” interchangeably, since our 2D views are all video frames.

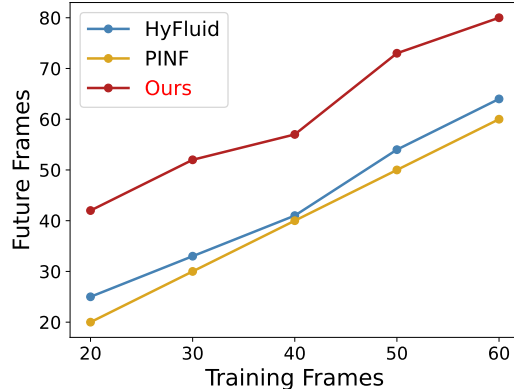


Figure 2. Our method is significantly more data-efficient compared with previous works (PINF [10], HyFluid [80]) on future prediction, over different numbers of initial training frames per input video (x-axis). We show the temporal index of reliably predicted future frames, using a peak signal-to-noise ratio (PSNR) threshold of 25, on the y-axis.

3. We provide comprehensive experiments and ablation studies (Section 4), and demonstrate that our method not only unlocks extreme data efficiency, but also achieves both improved reconstruction error and visual quality for fluids in the real world.

## 2. Preliminary

### 2.1. Inferring Fluid Fields from Videos

Our method is developed to work with HyFluid [80], which infers neural fluid fields (density and velocity) from videos.

**Problem Definition.** Given videos of smoke rising upwards (Figure 1, left), with the number of frames (views) in each video denoted by  $n_f$ , HyFluid aims to infer the density field  $\sigma(x, y, z, t)$  and the underlying velocity field  $\mathbf{u}(x, y, z, t) = (v_x, v_y, v_z)$  of the smoke, both parameterized by deep networks.

The  $n_f$  is set to 120 by default in HyFluid. For the density field  $\sigma(x, y, z, t)$ , HyFluid randomly samples camera rays  $(x, y, z, t)$  and reconstructs the density field using a 4D extension of iNGP [46], which accelerates the neural rendering with multiscale hash encoding of spatiotemporal positions. During training, this reconstructed density field is optimized by comparing input and rendered views via differentiable volume rendering. This is illustrated in the bottom half of Figure 4. Similarly, the velocity field  $\mathbf{u}(x, y, z, t)$  is inferred by another iNGP model, and is supervised by physics-informed losses that enforce the preservation of density for incompressible flows and divergence-free velocity.

During inference, the density field is used to render the visual appearance of the smoke, and the learned velocity

field can be used to advect (evolve) the density over temporal steps for both *re-simulation* (interpolation of the temporal range seen during training) and *future prediction* (extrapolation of unseen future temporal ranges).

**ScalarFlow: Smoke Videos with Calibrated Cameras.** Recent works on reconstructions of neural fluid fields focus on studying the ScalarFlow dataset [16]: a comprehensive collection of volumetric reconstructions of real-world smoke plumes (Figure 1 left). It encompasses a wide array of complex, buoyancy-driven flows rising upwards that transition into turbulence, capturing observable scalar transport processes. To the best of our knowledge, ScalarFlow is by far the best-calibrated dataset on real-world fluid (smoke) dynamics.

## 2.2. SciML Foundation Model

For time-dependent PDEs, the solution is a mapping from the joint of a spatial and temporal domain to the dynamics of the physical system (e.g. density, velocity, vorticity of the fluid at a certain spatiotemporal location):  $\mathbf{v} := \mathcal{T} \times \mathcal{S} \rightarrow \mathbb{R}^d$ . In current literature [38, 39, 43, 61], the **forward modeling** operator  $\mathcal{N}$  computes the PDE solution given  $T_{in} \in \mathbb{Z}^+$  consecutive previous timesteps:  $\mathcal{N} := \mathbf{v}(t - T_{in} \cdot \Delta t, \cdot), \dots, \mathbf{v}(t - \Delta t, \cdot) \mapsto \mathbf{v}(t, \cdot)$ , where  $\Delta t$  is the granularity of the temporal grid. This enables finite-difference approximations of the temporal derivatives of PDEs. See Figure 3 for an illustration.

SciML aims to find ML-based surrogate models for forward modeling by learning an approximation from data  $\mathcal{N}_\phi \simeq \mathcal{N}$  ( $\phi$  for learnable parameters). To optimize  $\mathcal{N}_\phi$ , we take a dataset  $\mathcal{D}$  comprising  $N$  discretized PDE simulations (“samples”)  $\mathcal{D} := \{\mathbf{v}^{(i)} \mid i = 1, \dots, N\}$ , and minimize a loss functional  $L$ , typically the normalized root of the mean squared error ( $\text{nRMSE} \equiv \frac{\|\mathbf{v}_{\text{pred}} - \mathbf{v}\|_2}{\|\mathbf{v}\|_2}$  where  $\mathbf{v}_{\text{pred}}$  is the prediction from  $\mathcal{N}_\phi$ ).

Traditionally, SciML models focus on learning simulation data from one PDE [38, 39, 41] with variants<sup>2</sup>. However, recent works explored and verified the benefits of scaling up the pretraining data to include diverse PDE systems, thus developing **SciML foundation models** [25, 26, 43, 51, 58, 60, 68, 79]. Intuitively, although these PDEs model very different physical systems, this “multi-tasking” strategy may: 1) implicitly enforce the learning of the compositionality of PDEs (which describe core components like nonlinear advection or diffusion in common and also augment specialized terms like buoyancy or system constraints), and 2) facilitate transfer learning and knowledge sharing across multiple PDE families.

<sup>2</sup>We can obtain variants with different physical parameters, boundary conditions, initial conditions, etc. Please read our supplement for details.

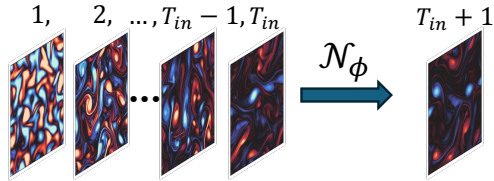


Figure 3. Forecasting by SciML foundation models [26, 43]. Given  $T_{in}$  previous steps, the model predicts the next step of the fluid dynamics (here, each frame shows the vorticity of the fluid).

## 3. Methods

In our work, we aim to reduce the number of video frames ( $n_f$ ) required by learning neural fluid fields, thereby improving data efficiency. In Figure 4, we overview our proposed framework<sup>3</sup>.

### 3.1. How to Utilize SciML Foundation Models for Inferring Real-World Fluid Fields?

Inspired by recent works [26, 43], we first develop our SciML foundation model as follows:

- 1. Architecture.** We adopt a 3D version of the Swin Transformer [40, 77] (6.5M parameters), a popular vision transformer architecture, as our foundation model<sup>4</sup>. It tokenizes input temporal 2D views ( $\mathbf{v}([t - T_{in} \cdot \Delta t : t - \Delta t], \cdot)$ ) with a 3D convolution layer, forwards through efficient windowed attentions, and predicts the next temporal step  $\mathbf{v}(t, \cdot)$ . Without loss of generality and following previous works [26, 43, 61], we choose  $T_{in} = 10$ . Tuning  $T_{in}$  may lead to better performance, but is not the focus of our method.
- 2. Multiphysics Pretraining.** We utilize the PDEBench dataset [61] for pretraining. Specifically, we pretrain our foundation model on the joint of diverse simulations of the following PDEs: both compressible and incompressible Navier-Stokes, shallow water, and reaction-diffusion. We sample each equation uniformly, zero-pad channels of PDEs with fewer variables, and match different PDE simulations to the same spatial resolution via interpolation. We will experimentally verify the benefits of this multiphysics pretraining in Section 4.4.
- 3. Fine-tuning.** After pretraining, we fine-tune on

<sup>3</sup>Our method directly interacts with only the density field of HyFluid, meanwhile its velocity field is implicitly improved via the density field.

<sup>4</sup>(1) Why not use larger model sizes? We will show that, even with a small model, we can already achieve strong improvements. Using larger models may further boost forecasting and extract more meaningful features, but this is not the focus of our work. Recent SciML foundation models also consider sizes smaller than 10M parameters [26, 60, 67, 79]. (2) Architecture choices: Without loss of generality, we adhere to the original design of the Swin Transformer and avoid introducing ad hoc modifications. Although recent works on SciML foundation models adopt different architectures [26, 43], the commonly shared aspect of these works is their joint multiphysics pretraining, not their deep network architectures.

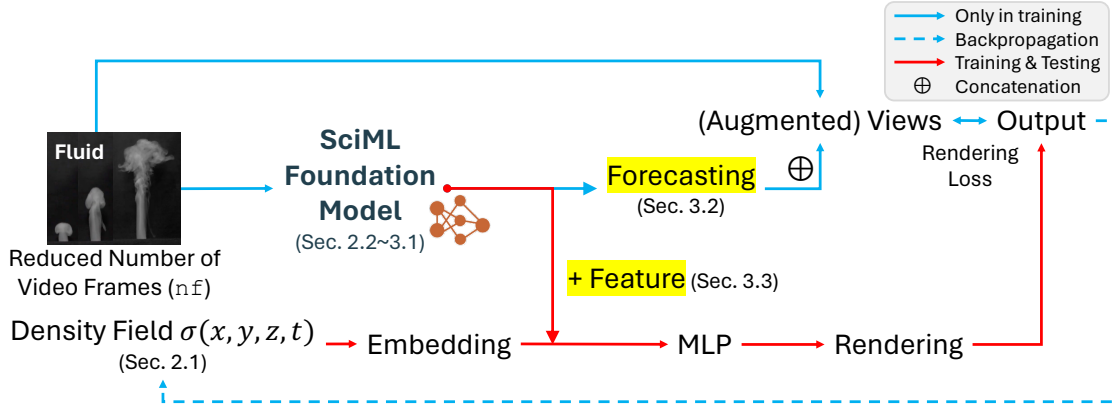


Figure 4. Overview: We improve the data efficiency (i.e., reduce the number of input fluid views “ $n_f$ ”) of learning neural fluid fields via the SciML foundation model. Given sparse input videos, we utilize our foundation model to: 1) forecast future steps to augment denser views for training (Section 3.2); 2) extract flow representations and aggregate into embeddings of fluid density fields (Section 3.3).

ScalarFlow<sup>5</sup>. Inspired by recent works [36, 49], we employ a curriculum schedule to encourage forecasting further temporal steps, gradually increasing autoregressive steps from 3 to 8 by 1 every 20 training epochs.

Both pretraining and fine-tuning use the nRMSE loss. We expect **two core benefits** of our SciML foundation model that can be utilized in the real world (highlighted with yellow in Figure 4):

1. **Strong Forecasting.** As our foundation model is pre-trained with the next-frame prediction, it can natively forecast precise future steps as augmented views of fluids to complement sparse videos (Section 3.2).
2. **Representation Learning.** As a data-driven approach similar to DINO [5, 48], the feature space constructed by our SciML foundation model can extract meaningful features of fluids to facilitate better generalization of 3D neural fluid fields (Section 3.3).

### 3.2. Co-Training via Foundation Model Forecasting

Given sparse smoke videos, one way to address data scarcity is to augment more views. We first study the forecasting performance of both our SciML foundation model and the neural fluid fields. As shown by two dotted curves in Figure 5 (“Foundation Model v0” vs. “HyFluid v0”), the forecasting quality of the foundation model is much better than the neural fluid fields.

To utilize the strong forecasting of our foundation model, we propose a collaborative training strategy for neural fluid fields. The core idea is to train the foundation model and neural fluid field with augmented views (Figure 6). We alternately concatenate the reliably predicted views (thresholded by  $PSNR=25$ ) from the foundation model or neural fluid field into the current training set, and fine-tune

each other. This collaborative training can also be viewed as a knowledge distillation from the foundation model to the neural fluid field in the output space. As shown by two dashed curves in Figure 5 (“Foundation Model v1”, “HyFluid v1”), the collaborative training enhances the forecasting of both models, and the final version of the neural fluid field (solid curve “HyFluid v2”) achieves much stronger future predictions. By achieving comparable PSNR with fewer input views, we demonstrate that our collaborative training can significantly improve the data efficiency of neural fluid fields.

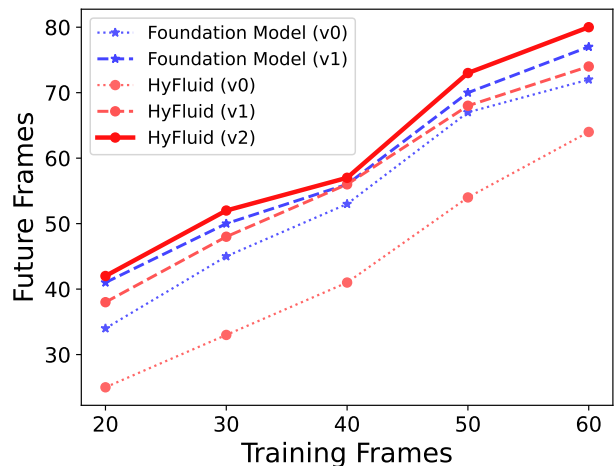


Figure 5. Collaborative training between HyFluid and foundation model via forecasting. “v0, v1, v2” match the corresponding models annotated in Figure 6. HyFluid can be progressively improved (v0→v1→v2) with more augmented views. Here we show future predictions over different numbers of initial training frames per input video (x-axis). We show the temporal index of reliable predicted future frames (thresholded by  $PSNR=25$ ) on the y-axis.

<sup>5</sup>The same set of sparse video views that will be used to train HyFluid.

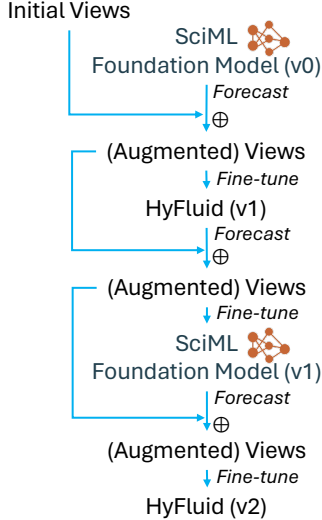


Figure 6. Collaborative training between HyFluid and our SciML foundation model via forecasting with augmented views. “v0, v1, v2” match the corresponding curves in Figure 5.

### 3.3. Feature Aggregation from Foundation Model

In addition to leveraging the augmented views via the foundation model’s forecasting, we further aggregate the learned representation from the foundation model into the neural fluid field. This can be viewed as a knowledge distillation from the foundation model to the neural fluid field in the feature space. We show our design of feature aggregation in Figure 7. This includes three steps:

1. For each camera ray  $(x_p, y_p, z_p)$ , we use the camera’s extrinsics and intrinsics to project the ray onto the position on image coordinates  $(h_{img}, w_{img})$ .
2. We reshape the sequence of tokens in our foundation model into 2D feature maps, and extract the feature vector corresponding to the camera ray via interpolating over the neighboring four feature coordinates. This feature vector is shared by all points sampled along the ray.
3. We use a two-layer MLP (with ReLU activation) to map the feature vector to the same feature dimensionality as the embedded features of the spatiotemporal coordinates of the density field, and sum them for aggregation.

During training, features are extracted from fluid views available in the videos. During testing, since videos are not accessible, the SciML foundation model extracts features based on views rendered by the density field from prior temporal steps. To extract features of frames before the temporal step at  $T_{in}$ , we use temporal-wise interpolation to supplement necessary frames as inputs to the foundation model.

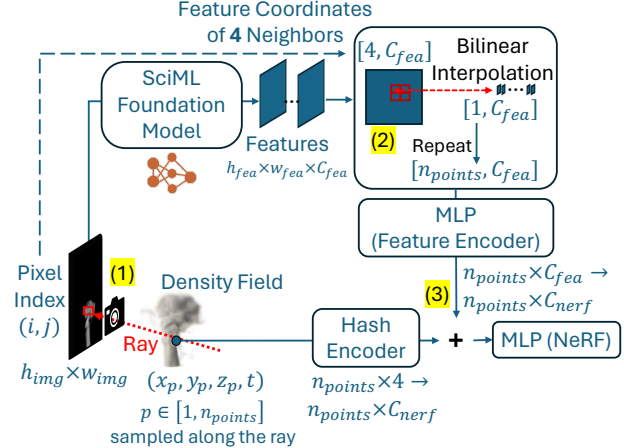


Figure 7. We aggregate representations learned by our SciML foundation model into HyFluid with three steps: (1) project from spatiotemporal location to the camera plane; (2) extract and interpolate neighboring features; (3) aggregate features from the foundation model into neural fields.

## 4. Experiments

### 4.1. Settings

**Datasets.** We use real captures from the ScalarFlow dataset [16], released in the repository of HyFluid. For each scene, there are five videos from five cameras fixed at positions evenly distributed across a  $120^\circ$  arc centered at the rising smoke. In each video, we consider the first  $n_f$  frames (where the smoke plumes upwards from the bottom), and adjust  $n_f$  to study our data efficiency. Each video has a resolution of  $1920 \times 1080$ . These videos have been post-processed to remove backgrounds. Following HyFluid, for each scene, we use four videos for training and hold one out for testing (i.e., as the ground-truth novel view).

**Evaluations.** We mainly compare with two previous works on neural fluid fields: PINF [10] and HyFluid [80]. Due to the lack of true 3D volume in ScalarFlow, we evaluate the reconstruction quality using view rendering. Following [80], we consider three tasks: novel view synthesis, re-simulation, and future prediction. In novel view synthesis, the density field is used to render smoke views from unseen camera parameters and spatial locations; thus, its quality is evaluated based on rendering accuracy. For re-simulation and future prediction, the learned velocity field is utilized to advect the density across temporal coordinates. Thus, the quality of the learned velocity field is assessed based on its effect on the density field. In our future prediction experiments, no model is ever trained with ground-truth future frames from the videos. We refer the reader to [80] for more details about these tasks. In this paper, we report the peak signal-noise ratio (PSNR) averaged over frames. We leave the structural similarity index measure (SSIM) and the perceptual metric LPIPS [82] in our supplement.

Table 1. Comparing PSNR (higher the better) of fluid field reconstruction by different methods. “ $nf$ ”: number of input training frames (views). For future prediction, we report the PSNR averaged over 20 future frames (i.e., frames with indices from  $nf+1 \rightarrow nf+20$ ).

Methods	Novel View Synthesis			Re-Simulation			Future Prediction		
	$nf=20$	$nf=40$	$nf=60$	$nf=20$	$nf=40$	$nf=60$	$nf=20$	$nf=40$	$nf=60$
PINF [10]	33.2246	31.8684	30.3225	24.284	24.8935	24.1265	21.7070	21.1770	20.8690
HyFluid [80]	33.5225	32.1226	31.6413	33.2671	32.9827	31.5625	23.9123	23.9832	23.8382
Ours	<b>34.9050</b>	<b>33.1838</b>	<b>32.7438</b>	<b>34.0704</b>	<b>33.7928</b>	<b>32.6558</b>	<b>28.5828</b>	<b>27.4636</b>	<b>27.7789</b>

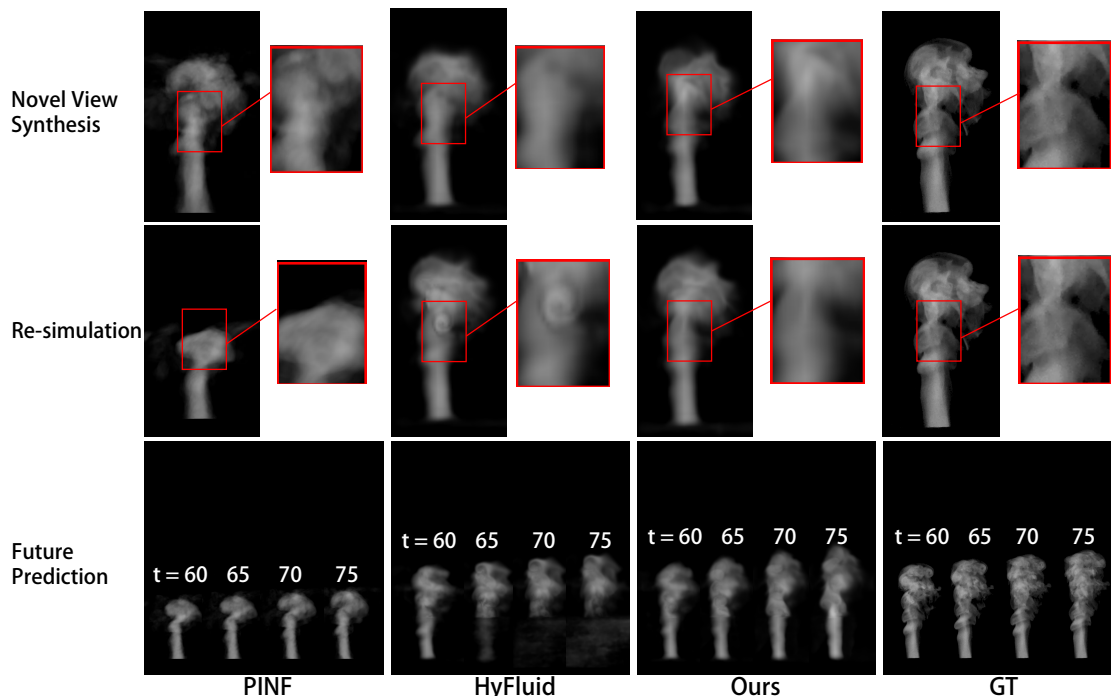


Figure 8. Visualization of novel view synthesis (top), re-simulation (middle), future prediction (bottom) on ScalarFlow [16] when 60 frames (per video) are used for training (i.e.,  $nf=60$ ). “GT”: ground truth.

## 4.2. Data-Efficiency Inference of Fluid Fields

We first report the inference of the fluid’s density fields. By default, HyFluid [80] and PINF [10] used 120 frames (i.e.,  $nf=120$ ) from each video during training. We consider using different numbers of sparse training views that are much fewer than those in HyFluid and PINF. As shown in Table 1, our PSNR consistently outperforms HyFluid and PINF under different sparse training views ( $nf$ ), across all three tasks<sup>6</sup>. More importantly, our method can predict much more reliable future frames with significantly reduced training views (Figure 2), achieving significant data efficiency.

## 4.3. More Realistic Visual Quality

Besides measuring the PSNR, it is vital to visually check the rendering quality of different methods. We show vi-

<sup>6</sup>PSNRs across different  $nf$ s are not comparable, since the numbers of testing views used to calculate PSNR are also adjusted to be equal to the numbers of training views.

ualizations in Figure 8. For novel view synthesis and re-simulation, our method recovers plausible details and avoids artifacts seen in HyFluid and PINF. Our ability to accurately reconstruct density fields further unlocks high-fidelity future predictions. Even with extremely sparse input views, our method is considerably more stable and robust than both HyFluid and PINF, which suffer from diverged density fields and weak forecasting. In contrast, our method preserves the original structure and maintains a natural upward flow.

## 4.4. Benefits of SciML Pretraining

As the core of our SciML foundation model is the joint pre-training on diverse PDE simulations (Section 2), it is critical to demonstrate the benefits of the domain knowledge from multiphysics. We provide our analysis below and identify two benefits.

Table 2. Benefit of multiphysics pretraining on the PSNR (higher the better) of fluid field reconstruction. “nf”: number of input training frames (views). For future prediction, we report the PSNR averaged over 20 future frames (i.e., frames with indices from  $nf+1 \rightarrow nf+20$ ).

Methods	Novel View Synthesis			Re-Simulation			Future Prediction		
	nf=20	nf=40	nf=60	nf=20	nf=40	nf=60	nf=20	nf=40	nf=60
No Pretraining	34.7700	32.8264	32.2896	<b>34.1157</b>	32.9699	32.5093	26.5795	25.9225	26.6141
+Multiphysics Pretraining	<b>34.9050</b>	<b>33.1838</b>	<b>32.7438</b>	34.0704	<b>33.7928</b>	<b>32.6558</b>	<b>28.5828</b>	<b>27.4636</b>	<b>27.7789</b>

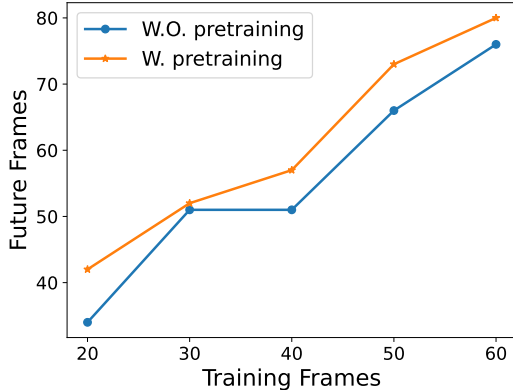


Figure 9. Benefit of multiphysics pretraining on future prediction over different numbers of initial training frames per input video (x-axis). We show the temporal index of reliable predicted future frames (thresholded by  $PSNR=25$ ) on y-axis.

**Improved generalization of neural fluid fields.** We compare the performance of neural fluid fields equipped with our foundation model, with and without multiphysics pretraining. As shown in Figure 9, the multiphysics pretraining can largely improve the data efficiency of neural fluid fields during future prediction. Moreover, over all three fluid reconstruction tasks, the utilization of multiphysics pretraining leads to much improved PSNR, as shown in Table 2. These results validate the necessity of the high-quality pretraining of our SciML foundation model.

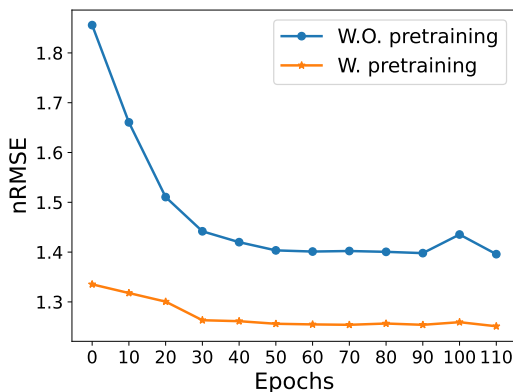


Figure 10. Multiphysics pretraining accelerates the convergence during fine-tuning of our SciML foundation model (on 40 initial frames from each of the four training videos in ScalarFlow).

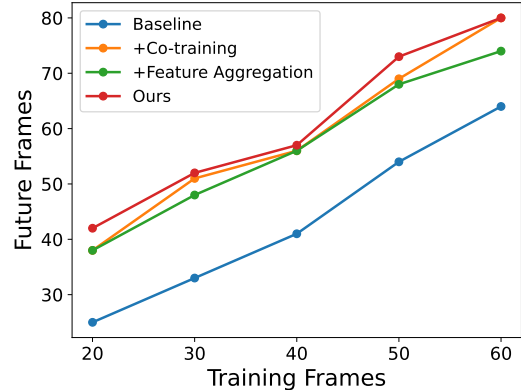


Figure 11. Ablation study of our decomposed methods on future prediction over different numbers of initial training frames per input video (x-axis). We show the temporal index of reliable predicted future frames (thresholded by  $PSNR=25$ ) on y-axis.

**Faster convergence during fine-tuning.** Multiphysics pretraining also enables fast convergence during fine-tuning on real-world fluid data. Despite gaps between PDE simulations and real-world fluid captures, the pretrained weights can still be quickly adapted to achieve accurate predictions and forecasting, as shown in Figure 10.

#### 4.5. Ablation Study

We further provide ablation studies on our decoupled framework to demonstrate the benefits of each individual component. As shown in Table 3 and Figure 11, both of our methods outperform the HyFluid baseline, with the combined approach achieving the best performance. For more ablation studies, please read our supplement.

### 5. Related works

#### 5.1. 3D Reconstruction of Fluid

To reconstruct 3D fluid phenomena from visual measurements, traditional approaches primarily utilized active sensing techniques [22, 28, 30] or particle imaging velocimetry (PIV) [2, 18]. While effective, these methods necessitated sophisticated and controlled laboratory environments, limiting their applicability. To circumvent these constraints, supervised view synthesis techniques were recently proposed. In [81], regularizers based on view interpolation and projection consistency were proposed to reconstruct fluid flow

Table 3. Ablation study of our methods on the PSNR (higher the better) of fluid field reconstruction. “nf”: number of input training frames (views). For future prediction, we report the PSNR averaged over 20 future frames (i.e., frames with indices from  $nf+1 \rightarrow nf+20$ ).

Methods	Novel View Synthesis			Re-Simulation			Future Prediction		
	nf=20	nf=40	nf=60	nf=20	nf=40	nf=60	nf=20	nf=40	nf=60
Co-training	34.5637	<b>33.1945</b>	32.3078	34.0342	33.1308	32.6052	28.0244	25.2019	26.8699
Feature Aggregation	33.8781	33.1796	<b>32.7645</b>	33.8782	33.2942	32.0876	26.5795	27.1271	25.6141
Ours	<b>34.9050</b>	33.1838	32.7438	<b>34.0704</b>	<b>33.7928</b>	<b>32.6558</b>	<b>28.5828</b>	<b>27.4636</b>	<b>27.7789</b>

from light tomography views. Franz et al.[19] proposed to reconstruct volumetric flow motion via a global transport formulation and differentiable rendering for end-to-end optimization. NeRFlow[14] learned 4D spatiotemporal representations of dynamic scenes by capturing the 3D occupancy, radiance, and dynamics of the scene while enforcing consistency across different modalities. PINF [10] was the first to propose reconstructing dynamic fluid phenomena by leveraging governing physics (Navier-Stokes equations) to train a continuous spatiotemporal scene representation with a neural radiance field. NeuroFluid [23] proposed a framework for a particle-driven neural renderer that integrates fluid physical properties into volume rendering and includes a particle transition model to minimize differences between rendered and observed fluid views. HyFluid [80] proposed hybrid neural fluid fields to jointly infer fluid density and velocity fields, using a set of physics-based losses to enforce physically plausible density and velocity fields. A vortex particle-based velocity approach was also introduced to model residual turbulence. However, none of these works explored the introduction of appropriate prior knowledge to achieve data efficiency and improve generalization.

## 5.2. Scientific Machine Learning

SciML, fueled by advancements in deep learning, models physical phenomena and differential equations [7, 8, 34, 35]. Physics-informed neural networks (PINNs)[20, 21, 52, 55, 85] aim to incorporate physics into neural networks by including the differential form of the PDE as an additional physics loss regularization term. However, this paradigm has been confined to specific PDE scenarios (e.g., fixed PDE coefficients). Moreover, recent work has highlighted several fundamental issues with PINN-based methods[17, 33]. In contrast, operator learning methods, including Fourier Neural Operators [32, 37, 38] and the Deep Operator Network [41], have made progress in approximating the solution operators of PDEs. Although these data-driven approaches show promise in learning PDE solutions, they rely on vast quantities of high-fidelity labeled data. Researchers have also explored generating synthetic PDE solutions to train SciML models [27]. More recently, SciML foundation models have been developed [25, 26, 43, 51, 58, 60, 68, 79] by scaling up training datasets to incorporate multiple PDE simulations. SciML foundation models aim

to encode common physical behaviors and enhance the generalization and scalability of SciML.

## 5.3. Foundation Models for 3D Reconstruction

“Vision foundation models” are large-scale models pre-trained on vast amounts of vision data, designed to generalize effectively across downstream vision tasks [5, 50, 53, 54, 56, 72, 76, 84]. CLIP [50] employed contrastive learning with extensive image-text data and achieved zero-shot performance across multiple tasks. DINO [5], exemplified self-supervised learning by achieving impressive object segmentation with minimal supervision, proving useful for tasks involving visual correspondence and recognition [3, 9, 44, 70]. Moreover, recent text-conditioned generative models, particularly diffusion models [13, 29, 47, 56], demonstrated exceptional image generation capabilities, with their learned feature spaces also serving recognition purposes, such as in semantic segmentation [4, 74]. However, in contrast to the well-established 2D foundation models, their 3D counterparts were hindered by the scarcity of large-scale annotated datasets and the limitations of current architectures [24, 57, 75]. In light of these challenges, researchers increasingly explored the potential of distilling 2D foundation model features into 3D space, exemplified by generalizable neural radiance fields (NeRFs) proposed to bridge this gap [6, 42, 62, 66, 71, 73, 78, 83].

## 6. Conclusions

In this work, we demonstrate that integrating SciML foundation models with neural fluid fields provides a substantial improvement in data efficiency and generalization for inferring 3D fluid fields. Through a collaborative training approach, our method leverages the foundation model’s forecasting capabilities to augment data, thereby reducing the reliance on extensive training views. Additionally, the aggregation of pretrained representations enables more accurate reconstructions of fluid dynamics from sparse video frames. The results indicate that this strategy not only enhances reconstruction quality but also achieves robust performance in novel view synthesis and future prediction. Our work highlights the practical applicability of SciML foundation models in real-world fluid dynamics, presenting a promising pathway for advancing data-efficient scientific modeling in complex, dynamic environments.



## References

- [1] Josh Achiam, Steven Adler, Sandhini Agarwal, Lama Ahmad, Ilge Akkaya, Florencia Leoni Aleman, Diogo Almeida, Janko Altenschmidt, Sam Altman, Shyamal Anadkat, et al. Gpt-4 technical report. [arXiv preprint arXiv:2303.08774](#), 2023. 2
- [2] Ronald J Adrian and Jerry Westerweel. [Particle image velocimetry](#). Number 30. Cambridge university press, 2011. 7
- [3] Shir Amir, Yossi Gandelsman, Shai Bagon, and Tali Dekel. Deep vit features as dense visual descriptors. [arXiv preprint arXiv:2112.05814](#), 2(3):4, 2021. 8
- [4] Dmitry Baranchuk, Ivan Rubachev, Andrey Voynov, Valentin Khrukov, and Artem Babenko. Label-efficient semantic segmentation with diffusion models. [arXiv preprint arXiv:2112.03126](#), 2021. 8
- [5] Mathilde Caron, Hugo Touvron, Ishan Misra, Herve Jegou, Julien Mairal, Piotr Bojanowski, and Armand Joulin. Emerging properties in self-supervised vision transformers. In [Proceedings of the IEEE/CVF international conference on computer vision](#), pages 9650–9660, 2021. 2, 4, 8
- [6] David Charatan, Sizhe Lester Li, Andrea Tagliasacchi, and Vincent Sitzmann. pixelsplat: 3d gaussian splats from image pairs for scalable generalizable 3d reconstruction. In [Proceedings of the IEEE/CVF Conference on Computer Vision and Pattern Recognition](#), pages 19457–19467, 2024. 2, 8
- [7] Tianping Chen and Hong Chen. Approximation capability to functions of several variables, nonlinear functionals, and operators by radial basis function neural networks. [IEEE Transactions on Neural Networks](#), 6(4):904–910, 1995. 8
- [8] Tianping Chen and Hong Chen. Universal approximation to nonlinear operators by neural networks with arbitrary activation functions and its application to dynamical systems. [IEEE transactions on neural networks](#), 6(4):911–917, 1995. 8
- [9] Subhabrata Choudhury, Iro Laina, Christian Rupprecht, and Andrea Vedaldi. Unsupervised part discovery from contrastive reconstruction. [Advances in Neural Information Processing Systems](#), 34:28104–28118, 2021. 8
- [10] Mengyu Chu, Lingjie Liu, Quan Zheng, Erik Franz, Hans-Peter Seidel, Christian Theobalt, and Rhaleb Zayer. Physics informed neural fields for smoke reconstruction with sparse data. [ACM Transactions on Graphics \(ToG\)](#), 41(4):1–14, 2022. 1, 2, 5, 6, 8, 14, 15
- [11] Yitong Deng, Hong-Xing Yu, Jiajun Wu, and Bo Zhu. Learning vortex dynamics for fluid inference and prediction. [arXiv preprint arXiv:2301.11494](#), 2023.
- [12] Yitong Deng, Hong-Xing Yu, Diyang Zhang, Jiajun Wu, and Bo Zhu. Fluid simulation on neural flow maps. [ACM Transactions on Graphics \(TOG\)](#), 42(6):1–21, 2023. 1
- [13] Prafulla Dhariwal and Alexander Nichol. Diffusion models beat gans on image synthesis. [Advances in neural information processing systems](#), 34:8780–8794, 2021. 8
- [14] Yilun Du, Yanan Zhang, Hong-Xing Yu, Joshua B Tenenbaum, and Jiajun Wu. Neural radiance flow for 4d view synthesis and video processing. In [2021 IEEE/CVF International Conference on Computer Vision \(ICCV\)](#), pages 14304–14314. IEEE Computer Society, 2021. 8
- [15] Abhimanyu Dubey, Abhinav Jauhri, Abhinav Pandey, Abhishek Kadian, Ahmad Al-Dahle, Aiesha Letman, Akhil Mathur, Alan Schelten, Amy Yang, Angela Fan, et al. The llama 3 herd of models. [arXiv preprint arXiv:2407.21783](#), 2024. 2
- [16] Marie-Lena Eckert, Kiwon Um, and Nils Thuerey. Scalarflow: a large-scale volumetric data set of real-world scalar transport flows for computer animation and machine learning. [ACM Transactions on Graphics \(TOG\)](#), 38(6):1–16, 2019. 1, 3, 5, 6, 16
- [17] C. Edwards. Neural networks learn to speed up simulations. [Communications of the ACM](#), 65(5):27–29, 2022. 8
- [18] Gerrit E Elsinga, Fulvio Scarano, Bernhard Wieneke, and Bas W van Oudheusden. Tomographic particle image velocimetry. [Experiments in fluids](#), 41(6):933–947, 2006. 7
- [19] Erik Franz, Barbara Solenthaler, and Nils Thuerey. Global transport for fluid reconstruction with learned self-supervision. In [Proceedings of the IEEE/CVF Conference on Computer Vision and Pattern Recognition](#), pages 1632–1642, 2021. 8
- [20] Han Gao, Luning Sun, and Jian-Xun Wang. Phygeonet: Physics-informed geometry-adaptive convolutional neural networks for solving parameterized steady-state pdes on irregular domain. [Journal of Computational Physics](#), 428:110079, 2021. 8
- [21] Nicholas Geneva and Nicholas Zabaras. Modeling the dynamics of pde systems with physics-constrained deep autoregressive networks. [Journal of Computational Physics](#), 403:109056, 2020. 8
- [22] Jinwei Gu, Shree K Nayar, Eitan Grinspun, Peter N Belhumeur, and Ravi Ramamoorthi. Compressive structured light for recovering inhomogeneous participating media. [IEEE transactions on pattern analysis and machine intelligence](#), 35(3):1–1, 2012. 7
- [23] Shanyan Guan, Huayu Deng, Yunbo Wang, and Xiaokang Yang. Neurofluid: Fluid dynamics grounding with particle-driven neural radiance fields. In [International Conference on Machine Learning](#), pages 7919–7929. PMLR, 2022. 1, 8
- [24] Huy Ha and Shuran Song. Semantic abstraction: Openworld 3d scene understanding from 2d vision-language models. [arXiv preprint arXiv:2207.11514](#), 2022. 8
- [25] Zhou Hang, Yuezhou Ma, Haixu Wu, Haowen Wang, and Mingsheng Long. Unisolver: Pde-conditional transformers are universal pde solvers. [arXiv preprint arXiv:2405.17527](#), 2024. 2, 3, 8
- [26] Zhongkai Hao, Chang Su, Songming Liu, Julius Berner, Chengyang Ying, Hang Su, Anima Anandkumar, Jian Song, and Jun Zhu. Dpot: Auto-regressive denoising operator transformer for large-scale pde pre-training. [arXiv preprint arXiv:2403.03542](#), 2024. 2, 3, 8, 17, 18
- [27] Erisa Hasani and Rachel A Ward. Generating synthetic data for neural operators. [arXiv preprint arXiv:2401.02398](#), 2024. 8
- [28] Tim Hawkins, Per Einarsson, and Paul Debevec. Acquisition of time-varying participating media. [ACM Transactions on Graphics \(ToG\)](#), 24(3):812–815, 2005. 7

- [29] Jonathan Ho, Ajay Jain, and Pieter Abbeel. Denoising diffusion probabilistic models. *Advances in neural information processing systems*, 33:6840–6851, 2020. 8
- [30] Yu Ji, Jinwei Ye, and Jingyi Yu. Reconstructing gas flows using light-path approximation. In *Proceedings of the IEEE Conference on Computer Vision and Pattern Recognition*, pages 2507–2514, 2013. 7
- [31] Dmitrii Kochkov, Jamie A Smith, Ayya Alieva, Qing Wang, Michael P Brenner, and Stephan Hoyer. Machine learning–accelerated computational fluid dynamics. *Proceedings of the National Academy of Sciences*, 118(21):e2101784118, 2021. 2
- [32] Nikola Kovachki, Zongyi Li, Burigede Liu, Kamyar Azizzadenesheli, Kaushik Bhattacharya, Andrew Stuart, and Anima Anandkumar. Neural operator: Learning maps between function spaces with applications to PDEs. *Journal of Machine Learning Research*, 24(89):1–97, 2023. 8
- [33] Aditi Krishnapriyan, Amir Gholami, Shandian Zhe, Robert Kirby, and Michael W Mahoney. Characterizing possible failure modes in physics-informed neural networks. *Advances in Neural Information Processing Systems*, 34:26548–26560, 2021. 8
- [34] Isaac E Lagaris, Aristidis Likas, and Dimitrios I Fotiadis. Artificial neural networks for solving ordinary and partial differential equations. *IEEE transactions on neural networks*, 9(5):987–1000, 1998. 8
- [35] Isaac E Lagaris, Aristidis C Likas, and Dimitris G Papa-georgiou. Neural-network methods for boundary value problems with irregular boundaries. *IEEE Transactions on Neural Networks*, 11(5):1041–1049, 2000. 8
- [36] Remi Lam, Alvaro Sanchez-Gonzalez, Matthew Willson, Peter Wirnsberger, Meire Fortunato, Ferran Alet, Suman Ravuri, Timo Ewalds, Zach Eaton-Rosen, Weihua Hu, et al. Graphcast: Learning skillful medium-range global weather forecasting. *arXiv preprint arXiv:2212.12794*, 2022. 4
- [37] Zongyi Li, Nikola Kovachki, Kamyar Azizzadenesheli, Burigede Liu, Andrew Stuart, Kaushik Bhattacharya, and Anima Anandkumar. Multipole graph neural operator for parametric partial differential equations. *Advances in Neural Information Processing Systems*, 33:6755–6766, 2020. 8
- [38] Zongyi Li, Nikola Borislavov Kovachki, Kamyar Azizzadenesheli, Burigede liu, Kaushik Bhattacharya, Andrew Stuart, and Anima Anandkumar. Fourier neural operator for parametric partial differential equations. In *International Conference on Learning Representations*, 2021. 2, 3, 8
- [39] Zongyi Li, Hongkai Zheng, Nikola Kovachki, David Jin, Haoxuan Chen, Burigede Liu, Kamyar Azizzadenesheli, and Anima Anandkumar. Physics-informed neural operator for learning partial differential equations. *arXiv preprint arXiv:2111.03794*, 2021. 3
- [40] Ze Liu, Yutong Lin, Yue Cao, Han Hu, Yixuan Wei, Zheng Zhang, Stephen Lin, and Baining Guo. Swin transformer: Hierarchical vision transformer using shifted windows. In *Proceedings of the IEEE/CVF international conference on computer vision*, pages 10012–10022, 2021. 3, 16
- [41] Lu Lu, Pengzhan Jin, and George Em Karniadakis. Deeponet: Learning nonlinear operators for identifying differen-  
tial equations based on the universal approximation theorem of operators. *arXiv preprint arXiv:1910.03193*, 2019. 3, 8
- [42] Mana Masuda, Jinhyung Park, Shun Iwase, Rawal Khrodkar, and Kris Kitani. Generalizable neural human renderer. *arXiv preprint arXiv:2404.14199*, 2024. 2, 8
- [43] Michael McCabe, Bruno Regalado-Saint Blancard, Liam Holden Parker, Ruben Ohana, Miles Cranmer, Alberto Bietti, Michael Eickenberg, Siavash Golkar, Gerard Krawezik, Francois Lanusse, et al. Multiple physics pretraining for physical surrogate models. *arXiv preprint arXiv:2310.02994*, 2023. 2, 3, 8, 17, 18
- [44] Luke Melas-Kyriazi, Christian Rupprecht, Iro Laina, and Andrea Vedaldi. Deep spectral methods: A surprisingly strong baseline for unsupervised semantic segmentation and localization. In *Proceedings of the IEEE/CVF Conference on Computer Vision and Pattern Recognition*, pages 8364–8375, 2022. 8
- [45] Gregoire Mialon, Quentin Garrido, Hannah Lawrence, Danyal Rehman, Yann LeCun, and Bobak Kiani. Self-supervised learning with lie symmetries for partial differential equations. *Advances in Neural Information Processing Systems*, 36:28973–29004, 2023. 2
- [46] Thomas Müller, Alex Evans, Christoph Schied, and Alexander Keller. Instant neural graphics primitives with a multiresolution hash encoding. *ACM transactions on graphics (TOG)*, 41(4):1–15, 2022. 2
- [47] Alexander Quinn Nichol and Prafulla Dhariwal. Improved denoising diffusion probabilistic models. In *International conference on machine learning*, pages 8162–8171. PMLR, 2021. 8
- [48] Maxime Oquab, Timothee Darcet, Theo Moutakanni, Huy Vo, Marc Szafraniec, Vasil Khalidov, Pierre Fernandez, Daniel Haziza, Francisco Massa, Alaaeldin El-Nouby, et al. Dinov2: Learning robust visual features without supervision. *arXiv preprint arXiv:2304.07193*, 2023. 2, 4
- [49] Jaideep Pathak, Shashank Subramanian, Peter Harrington, Sanjeev Raja, Ashesh Chattopadhyay, Morteza Mardani, Thorsten Kurth, David Hall, Zongyi Li, Kamyar Azizzadenesheli, et al. Fourcastnet: A global data-driven high-resolution weather model using adaptive fourier neural operators. *arXiv preprint arXiv:2202.11214*, 2022. 1, 2, 4
- [50] Alec Radford, Jong Wook Kim, Chris Hallacy, Aditya Ramesh, Gabriel Goh, Sandhini Agarwal, Girish Sastry, Amanda Askell, Pamela Mishkin, Jack Clark, et al. Learning transferable visual models from natural language supervision. In *International conference on machine learning*, pages 8748–8763. PMLR, 2021. 2, 8
- [51] Md Ashiqur Rahman, Robert Joseph George, Mogab Elleithy, Daniel Leibovici, Zongyi Li, Boris Bonev, Colin White, Julius Berner, Raymond A Yeh, Jean Kossaifi, et al. Pretraining codomain attention neural operators for solving multi-physics pdes. *arXiv preprint arXiv:2403.12553*, 2024. 2, 3, 8
- [52] Maziar Raissi, Paris Perdikaris, and George E Karniadakis. Physics-informed neural networks: A deep learning framework for solving forward and inverse problems involving nonlinear partial differential equations. *Journal of Computational physics*, 378:686–707, 2019. 8

- [53] Aditya Ramesh, Mikhail Pavlov, Gabriel Goh, Scott Gray, Chelsea Voss, Alec Radford, Mark Chen, and Ilya Sutskever. Zero-shot text-to-image generation. In *International conference on machine learning*, pages 8821–8831. Pmlr, 2021. 8
- [54] Aditya Ramesh, Prafulla Dhariwal, Alex Nichol, Casey Chu, and Mark Chen. Hierarchical text-conditional image generation with clip latents. *arXiv preprint arXiv:2204.06125*, 1(2):3, 2022. 8
- [55] Pu Ren, Chengping Rao, Yang Liu, Jian-Xun Wang, and Hao Sun. Phycnet: Physics-informed convolutional-recurrent network for solving spatiotemporal pdes. *Computer Methods in Applied Mechanics and Engineering*, 389:114399, 2022. 8
- [56] Robin Rombach, Andreas Blattmann, Dominik Lorenz, Patrick Esser, and Björn Ommer. High-resolution image synthesis with latent diffusion models. In *Proceedings of the IEEE/CVF conference on computer vision and pattern recognition*, pages 10684–10695, 2022. 8
- [57] David Rozenberszki, Or Litany, and Angela Dai. Language-grounded indoor 3d semantic segmentation in the wild. In *European Conference on Computer Vision*, pages 125–141. Springer, 2022. 8
- [58] Junhong Shen, Tanya Marwah, and Ameet Talwalkar. Ups: Efficiently building foundation models for pde solving via cross-modal adaptation. In *ICML 2024 AI for Science Workshop*. 2, 3, 8
- [59] Shashank Subramanian, Peter Harrington, Kurt Keutzer, Wahid Bhimji, Dmitriy Morozov, Michael W Mahoney, and Amir Gholami. Towards foundation models for scientific machine learning: Characterizing scaling and transfer behavior. *arXiv preprint arXiv:2306.00258*, 2023. 2
- [60] Jingmin Sun, Yuxuan Liu, Zecheng Zhang, and Hayden Schaeffer. Towards a foundation model for partial differential equation: Multi-operator learning and extrapolation. *arXiv preprint arXiv:2404.12355*, 2024. 2, 3, 8
- [61] Makoto Takamoto, Timothy Praditia, Raphael Leiteritz, Daniel MacKinlay, Francesco Alesiani, Dirk Pflüger, and Mathias Niepert. Pdebench: An extensive benchmark for scientific machine learning. *Advances in Neural Information Processing Systems*, 35:1596–1611, 2022. 2, 3, 16, 17
- [62] Songlin Tang, Wenjie Pei, Xin Tao, Tanghui Jia, Guangming Lu, and Yu-Wing Tai. Scene-generalizable interactive segmentation of radiance fields. In *Proceedings of the 31st ACM International Conference on Multimedia*, pages 6744–6755, 2023. 2, 8
- [63] Nils Thuerey, Konstantin Weissenow, Lukas Prantl, and Xianguyu Hu. Deep learning methods for reynolds-averaged navier–stokes simulations of airfoil flows. *AIAA Journal*, 58(1):25–36, 2020. 1
- [64] Hugo Touvron, Thibaut Lavril, Gautier Izacard, Xavier Martinet, Marie-Anne Lachaux, Timothee Lacroix, Baptiste Rozière, Naman Goyal, Eric Hambro, Faisal Azhar, et al. Llama: Open and efficient foundation language models. *arXiv preprint arXiv:2302.13971*, 2023. 2
- [65] Hugo Touvron, Louis Martin, Kevin Stone, Peter Albert, Amjad Almahairi, Yasmine Babaei, Nikolay Bashlykov, Soumya Batra, Prajjwal Bhargava, Shruti Bhosale, et al. Llama 2: Open foundation and fine-tuned chat models. *arXiv preprint arXiv:2307.09288*, 2023. 2
- [66] Peihao Wang, Zhiwen Fan, Zhangyang Wang, Hao Su, Ravi Ramamoorthi, et al. Lift3d: Zero-shot lifting of any 2d vision model to 3d. In *Proceedings of the IEEE/CVF Conference on Computer Vision and Pattern Recognition*, pages 21367–21377, 2024. 2, 8
- [67] Sifan Wang, Jacob H Seidman, Shyam Sankaran, Hanwen Wang, George J Pappas, and Paris Perdikaris. Cvit: Continuous vision transformer for operator learning. *arXiv preprint arXiv:2405.13998*, 2024. 3
- [68] Tian Wang and Chuang Wang. Latent neural operator pre-training for solving time-dependent pdes. *arXiv preprint arXiv:2410.20100*, 2024. 2, 3, 8
- [69] Xiaokun Wang, Yanrui Xu, Sinuo Liu, Bo Ren, Jiri Kosinka, Alexandru C Telea, Jiamin Wang, Chongming Song, Jian Chang, Chenfeng Li, et al. Physics-based fluid simulation in computer graphics: Survey, research trends, and challenges. *Computational Visual Media*, pages 1–56, 2024. 1
- [70] Yangtao Wang, Xi Shen, Shell Xu Hu, Yuan Yuan, James L Crowley, and Dominique Vaufreydaz. Self-supervised transformers for unsupervised object discovery using normalized cut. In *Proceedings of the IEEE/CVF Conference on Computer Vision and Pattern Recognition*, pages 14543–14553, 2022. 8
- [71] Yixuan Wang, Mingtong Zhang, Zhuoran Li, Tarik Kelestmur, Katherine Rose Driggs-Campbell, Jiajun Wu, Li Fei-Fei, and Yunzhu Li. Dynamic 3d descriptor fields for zero-shot generalizable rearrangement. In *8th Annual Conference on Robot Learning*, 2024. 2, 8
- [72] Chen Wei, Haoqi Fan, Saining Xie, Chao-Yuan Wu, Alan Yuille, and Christoph Feichtenhofer. Masked feature prediction for self-supervised visual pre-training. In *Proceedings of the IEEE/CVF Conference on Computer Vision and Pattern Recognition*, pages 14668–14678, 2022. 8
- [73] Christopher Wewer, Kevin Raj, Eddy Ilg, Bernt Schiele, and Jan Eric Lenssen. latentsplat: Autoencoding variational gaussians for fast generalizable 3d reconstruction. *arXiv preprint arXiv:2403.16292*, 2024. 2, 8
- [74] Julia Wolleb, Robin Sandkühler, Florentin Bieder, Philippe Valmaggia, and Philippe C Cattin. Diffusion models for implicit image segmentation ensembles. In *International Conference on Medical Imaging with Deep Learning*, pages 1336–1348. PMLR, 2022. 8
- [75] Xiaoshi Wu, Hadar Averbuch-Elor, Jin Sun, and Noah Snavely. Towers of babel: Combining images, language, and 3d geometry for learning multimodal vision. In *Proceedings of the IEEE/CVF International Conference on Computer Vision*, pages 428–437, 2021. 8
- [76] Zhenda Xie, Yutong Lin, Zhuliang Yao, Zheng Zhang, Qi Dai, Yue Cao, and Han Hu. Self-supervised learning with swin transformers. *arXiv preprint arXiv:2105.04553*, 2021. 8
- [77] Yu-Qi Yang, Yu-Xiao Guo, Jian-Yu Xiong, Yang Liu, Hao Pan, Peng-Shuai Wang, Xin Tong, and Baining Guo. Swin3d: A pretrained transformer backbone for 3d in-

- door scene understanding. arXiv preprint arXiv:2304.06906, 2023. 3, 16
- [78] Jianglong Ye, Naiyan Wang, and Xiaolong Wang. Featurenerf: Learning generalizable nerfs by distilling foundation models. In Proceedings of the IEEE/CVF International Conference on Computer Vision, pages 8962–8973, 2023. 2, 8
- [79] Zhanhong Ye, Xiang Huang, Leheng Chen, Hongsheng Liu, Zidong Wang, and Bin Dong. Pdeformer: Towards a foundation model for one-dimensional partial differential equations. arXiv preprint arXiv:2402.12652, 2024. 2, 3, 8
- [80] Hong-Xing Yu, Yang Zheng, Yuan Gao, Yitong Deng, Bo Zhu, and Jiajun Wu. Inferring hybrid neural fluid fields from videos. Advances in Neural Information Processing Systems, 36, 2024. 1, 2, 5, 6, 8, 13, 14, 15
- [81] Guangming Zang, Ramzi Idoughi, Congli Wang, Anthony Bennett, Jianguo Du, Scott Skeen, William L Roberts, Peter Wonka, and Wolfgang Heidrich. Tomofluid: Reconstructing dynamic fluid from sparse view videos. In Proceedings of the IEEE/CVF Conference on Computer Vision and Pattern Recognition, pages 1870–1879, 2020. 7
- [82] Richard Zhang, Phillip Isola, Alexei A Efros, Eli Shechtman, and Oliver Wang. The unreasonable effectiveness of deep features as a perceptual metric. In Proceedings of the IEEE conference on computer vision and pattern recognition, pages 586–595, 2018. 5, 15
- [83] Xiaoshuai Zhang, Zhicheng Wang, Howard Zhou, Soham Ghosh, Danushen Gnanapragasam, Varun Jampani, Hao Su, and Leonidas Guibas. Condense: Consistent 2d/3d pre-training for dense and sparse features from multi-view images. arXiv preprint arXiv:2408.17027, 2024. 8
- [84] Shuai Feng Zhi, Tristan Laidlow, Stefan Leutenegger, and Andrew J Davison. In-place scene labelling and understanding with implicit scene representation. In Proceedings of the IEEE/CVF International Conference on Computer Vision, pages 15838–15847, 2021. 8
- [85] Yin Hao Zhu, Nicholas Zabaras, Phaedon-Stelios Koutsourakis, and Paris Perdikaris. Physics-constrained deep learning for high-dimensional surrogate modeling and uncertainty quantification without labeled data. Journal of Computational Physics, 394:56–81, 2019. 8

## 7. More Results

### 7.1. Justifications for Using $\text{PSNR}=25$ as the Threshold for Reliable Future Predictions

In our work, we mainly use  $\text{PSNR}=25$  as the threshold for determining reliable future predictions. As shown in Figure 12 left, the  $\text{PSNR}$  of forecasted frames decreases when we make further predictions, suggesting different possible  $\text{PSNR}$  thresholds (i.e., any future frames of  $\text{PSNR}$  below the threshold will be considered as unreliable with bad quality). Here, we provide justifications that this threshold is appropriate on ScalarFlow.

First, as shown in three subplots to the right in Figure 12, our data efficiency and improvements persist with different  $\text{PSNR}$  thresholds, indicating that using different thresholds will not change our conclusion.

Second, when we visualize the rendering quality of future frames with different  $\text{PSNR}$ s (Figure 13), we can see that, both frames with  $\text{PSNR}$  25 and 27 are of high visual quality, whereas the frame with  $\text{PSNR}=23$  is much visually worse. This implies that choosing the threshold as  $\text{PSNR} = 25$  is sufficient to characterize reliable reconstructions, but 23 already indicates bad qualities.

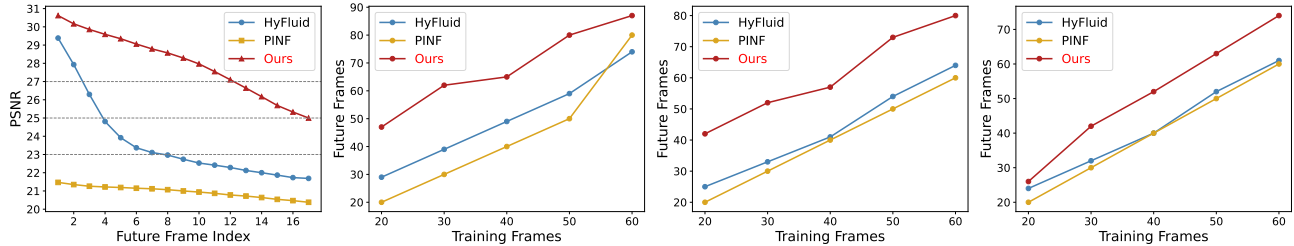


Figure 12. Justification for using  $\text{PSNR}=25$  as the threshold for reliable future predictions. **Left:**  $\text{PSNR}$ s of predicted future frames naturally decrease over longer time steps (results obtained with initial training frames  $n_f=40$ ). **Right three plots:** number of predicted future frames (y-axis) thresholded with different  $\text{PSNR}$  (23, 25, 27) over different numbers of initial training frames per input video (x-axis).

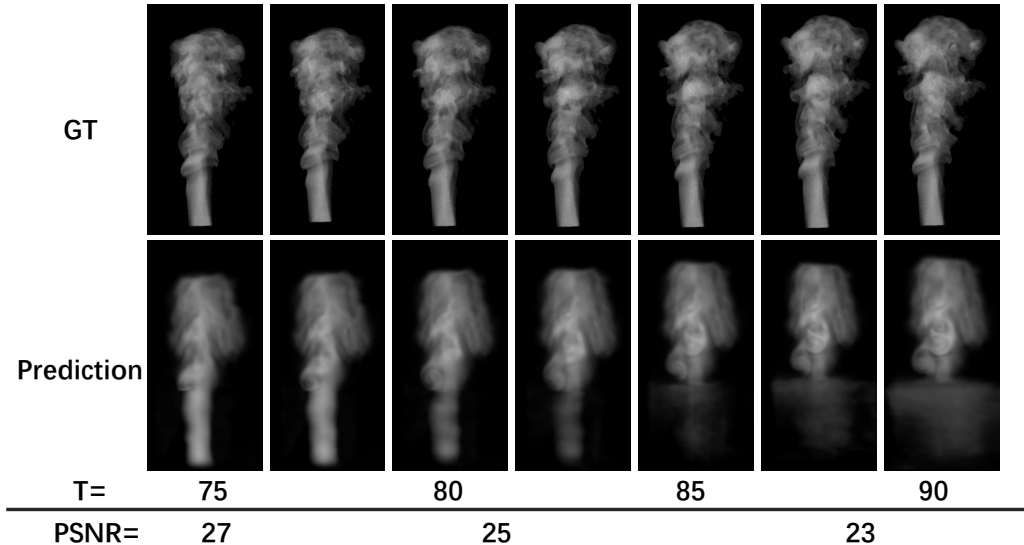


Figure 13. Justification for using  $\text{PSNR}=25$  as the threshold by comparing visualizations of our predicted future frames with different  $\text{PSNR}$ s. From left to right:  $\text{PSNR}$  progressively drops from 27 to 23. We use 60 initial frames (per video) for training in this example (i.e.,  $n_f=60$ ). “GT”: ground truth.

### 7.2. HyFluid with More Network Parameters

To demonstrate that our improvements are from the pretrained SciML foundation model instead of extra network parameters, we further compare with HyFluid of a larger model size. Our SciML foundation model has 6.5M parameters. The original density or velocity field in HyFluid [80] each has 14.9M parameters. To ensure a fairer comparison, we train an enlarged HyFluid model with both the density and velocity fields increased to 20.5M parameters. As shown in Table 4 and Figure 14, our method can largely outperform the HyFluid of a larger model size, confirming that our benefit is not rooted in more network parameters.

Table 4. PSNR (higher the better) of HyFluid with more network parameters. “nf”: number of input training frames (views). For future prediction, we report the PSNR averaged over 20 future frames (i.e., frames with indices from  $nf+1 \rightarrow nf+20$ ).

Methods	Novel View Synthesis			Re-Simulation			Future Prediction		
	nf=20	nf=40	nf=60	nf=20	nf=40	nf=60	nf=20	nf=40	nf=60
HyFluid [80]	33.5225	32.1226	31.6413	33.2671	32.9827	31.5625	23.9123	23.9832	23.8382
HyFluid Large	34.4745	32.3697	<b>32.8430</b>	<b>34.1626</b>	33.0153	32.4680	24.1039	24.2146	24.0630
Ours	<b>34.9050</b>	<b>33.1838</b>	32.7438	34.0704	<b>33.7928</b>	<b>32.6558</b>	<b>28.5828</b>	<b>27.4636</b>	<b>27.7789</b>

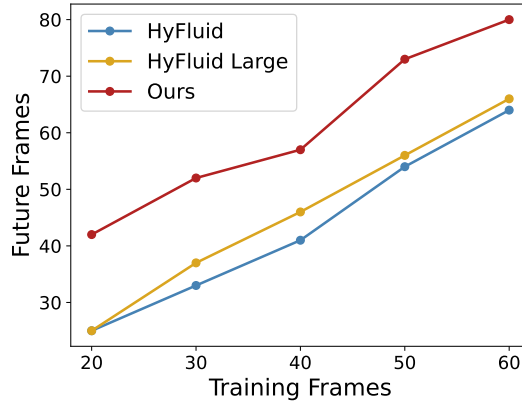


Figure 14. Comparing with HyFluid of even a larger model size, our method is still more data-efficient on future prediction, over different numbers of initial training frames per input video (x-axis). We show the temporal index of reliably predicted future frames, using a peak signal-to-noise ratio (PSNR) threshold of 25, on the y-axis.

### 7.3. Random Seeds and Standard Deviations

We further compare different methods considering standard deviations from random runs, in Table 5 and Figure 15. Our confidence is comparable with previous methods.

Table 5. We report standard deviations (3 random runs) of PSNR (higher the better) by different methods. “nf”: number of input training frames (views). For future prediction, we report the PSNR averaged over 20 future frames (i.e., frames with indices from  $nf+1 \rightarrow nf+20$ ).

Methods	Novel View Synthesis			Re-Simulation			Future Prediction		
	nf=20	nf=40	nf=60	nf=20	nf=40	nf=60	nf=20	nf=40	nf=60
PINF [10]	33.45 ( $\pm 0.22$ )	31.05 ( $\pm 1.14$ )	30.90 ( $\pm 0.44$ )	24.28 ( $\pm 0.00$ )	24.86 ( $\pm 0.06$ )	24.08 ( $\pm 0.07$ )	21.71 ( $\pm 0.00$ )	20.85 ( $\pm 0.01$ )	20.67 ( $\pm 0.03$ )
HyFluid [80]	33.83 ( $\pm 0.08$ )	33.32 ( $\pm 0.06$ )	32.84 ( $\pm 0.14$ )	33.89 ( $\pm 0.62$ )	33.27 ( $\pm 0.23$ )	32.02 ( $\pm 0.20$ )	25.22 ( $\pm 1.04$ )	23.98 ( $\pm 0.05$ )	23.66 ( $\pm 0.12$ )
Ours	<b>34.50</b> ( $\pm 0.44$ )	<b>33.48</b> ( $\pm 0.20$ )	<b>32.84</b> ( $\pm 0.14$ )	<b>34.34</b> ( $\pm 0.65$ )	<b>33.36</b> ( $\pm 0.07$ )	<b>32.42</b> ( $\pm 0.23$ )	<b>27.59</b> ( $\pm 0.24$ )	<b>28.36</b> ( $\pm 0.87$ )	<b>27.76</b> ( $\pm 0.09$ )

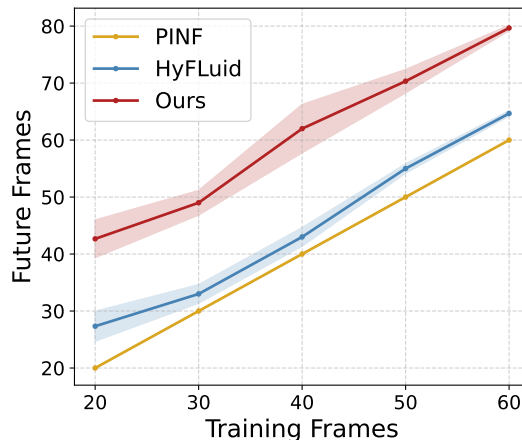


Figure 15. With high confidence (standard deviations as shaded areas), our method is significantly more data-efficient compared with previous works (PINF [10], HyFLuid [80]) on future prediction, over different numbers of initial training frames per input video (x-axis). We show the temporal index of reliably predicted future frames, using a peak signal-to-noise ratio (PSNR) threshold of 25, on the y-axis.

### 7.4. Training with More Initial Views

We further consider more numbers of initial views (larger  $nf$ ). We show our results in Table 6 and Figure 16. Again, our method consistently outperforms HyFluid [80] and PINF [10] on more initial frames.

Table 6. The PSNR (higher the better) of our method outperforms previous works over more initial numbers of training views ( $nf$ ). For future prediction, we report the PSNR averaged over 20 future frames (i.e., frames with indices from  $nf+1 \rightarrow nf+20$ ).

Methods	Novel View Synthesis			Re-Simulation			Future Prediction		
	$nf=70$	$nf=80$	$nf=90$	$nf=70$	$nf=80$	$nf=90$	$nf=70$	$nf=80$	$nf=90$
PINF [10]	31.2037	30.1842	29.7270	24.1510	24.3188	25.0177	21.0880	21.7535	22.8965
HyFluid [80]	32.5832	32.2781	32.3921	31.8151	31.4773	30.4726	21.7711	19.9964	21.2751
Ours	<b>32.8751</b>	<b>32.5497</b>	<b>32.4748</b>	<b>31.9859</b>	<b>31.5959</b>	<b>31.1382</b>	<b>30.9439</b>	<b>26.6234</b>	<b>26.6165</b>

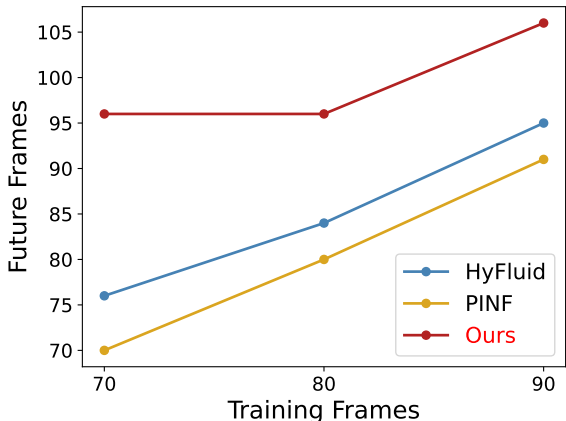


Figure 16. With more initial training frames per video ( $nf$ , x-axis), our method is still consistently more data-efficient compared with previous works (PINF [10], HyFluid [80]) on future prediction. We show the temporal index of reliably predicted future frames, using a peak signal-to-noise ratio (PSNR) threshold of 25, on the y-axis.

### 7.5. SSIM and LPIPS

Beyond PSNR, we further report the structural similarity index measure (SSIM) in Table 7 and the perceptual metric LPIPS [82] in Table 8. Our method is still shown to perform better based on these two additional metrics.

Table 7. Comparing SSIM (higher the better) of fluid field reconstruction by different methods. “ $nf$ ”: number of input training frames (views). For future prediction, we report the SSIM averaged over 20 future frames (i.e., frames with indices from  $nf+1 \rightarrow nf+20$ ).

Methods	Novel View Synthesis			Re-Simulation			Future Prediction		
	$nf=20$	$nf=40$	$nf=60$	$nf=20$	$nf=40$	$nf=60$	$nf=20$	$nf=40$	$nf=60$
PINF [10]	0.9688	0.9648	0.9412	0.9759	0.9530	0.9346	0.9471	<b>0.9046</b>	<b>0.8796</b>
HyFluid [80]	0.9770	<b>0.9741</b>	0.9616	0.9678	0.9667	0.9665	0.9086	0.8872	0.8686
Ours	<b>0.9812</b>	0.9644	<b>0.9645</b>	<b>0.9818</b>	<b>0.9677</b>	<b>0.9693</b>	<b>0.9526</b>	0.8963	0.8752

Table 8. Comparing LPIPS [82] (smaller the better) of fluid field reconstruction by different methods. “ $nf$ ”: number of input training frames (views). For future prediction, we report the LPIPS averaged over 20 future frames (i.e., frames with indices from  $nf+1 \rightarrow nf+20$ ).

Methods	Novel View Synthesis			Re-Simulation			Future Prediction		
	$nf=20$	$nf=40$	$nf=60$	$nf=20$	$nf=40$	$nf=60$	$nf=20$	$nf=40$	$nf=60$
PINF [10]	0.0454	0.0501	0.0682	0.0605	0.0728	0.0889	0.1066	0.1396	0.1539
HyFluid [80]	0.0323	<b>0.0395</b>	0.0611	0.0385	<b>0.0470</b>	0.0637	0.0922	0.1228	0.1489
Ours	<b>0.0293</b>	0.0478	<b>0.0567</b>	<b>0.0296</b>	0.0474	<b>0.0565</b>	<b>0.0625</b>	<b>0.1075</b>	<b>0.1315</b>

## 8. Implementation Details of SciML Foundation Model

### 8.1. Architecture

To develop our SciML foundation model, we follow the architecture design of 3D Swin Transformer in [40, 77]. We show our architecture in Figure 17. Specifically, after the tokenization layer (3D convolution) and patch embedding, we have 18 window attention blocks with a window size of (8,7,7).

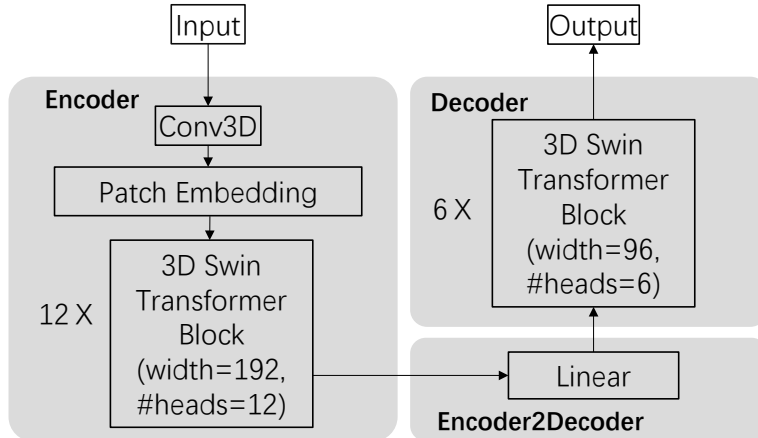


Figure 17. Visualizations of our SciML foundation model architecture (3D Swin Transformer).

### 8.2. Pretraining and Fine-tuning Settings

We summarize the pretraining and fine-tuning settings of our SciML foundation model in Table 9. During both multiphysics pretraining on PDEBench [61] and fine-tuning on ScalarFlow [16], all inputs are interpolated to a spatial resolution of  $224 \times 224$ .

Table 9. Summary of multiphysics pretraining and fine-tuning settings for our SciML foundation model. “LR”: learning rate. “BS”: batch size. “Rollout”: rollout steps for autoregressive predictions. “v0” and “v1” correspond to fine-tuning foundation models in Figure 5 and 6 in our main paper.

	LR	BS	Optimizer	Scheduler	Epochs	Rollout
Pretraining	0.1	4	SGD	Cosine	500	1
Fine-tuning v0	0.1	1	SGD	Cosine	200	Increase from 3 to 8 by 1 every 20 epochs
Fine-tuning v1	0.1	1	SGD	Cosine	100	8

### 8.3. Feature Extraction for $t < T_{in}$ with Temporal Interpolation

For feature aggregation, during testing, since videos are not accessible, our SciML foundation model extracts features based on views rendered by the density field from prior temporal steps. To extract features of frames for temporal steps before  $T_{in}$ , we use temporal-wise interpolation to supplement necessary frames as inputs to the foundation model. Specifically, we bi-linearly interpolate the input views from  $t$  to  $T_{in}$  steps and create  $T_{in} - t$  pseudo-views, as illustrated in Figure 18.

### 8.4. Pretraining of SciML Foundation Model

#### 8.4.1. PDEs

We summarize PDEs included in our multiphysics pretraining as below.

**Reaction-Diffusion.** The Reaction-Diffusion equation models an activator-inhibitor system, which typically happens in the dynamics of chemistry, biology, and ecology. The activator  $u$  promotes its own production, and the inhibitor  $v$  acts to



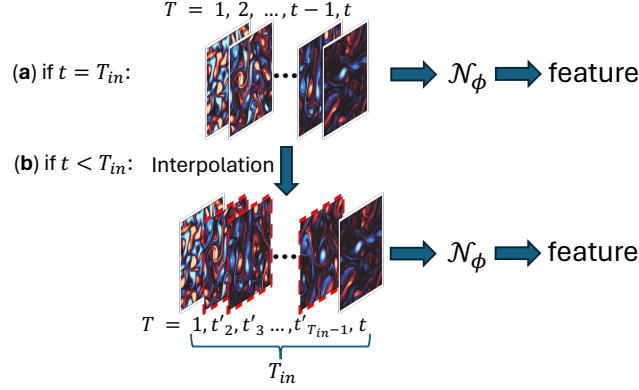


Figure 18. Forecasting by SciML foundation models ( $\mathcal{N}$  parameterized by  $\phi$ ) [26, 43]. (a) If  $t = T_{in}$  (i.e., we have sufficient input frames from previous steps), the model predicts the next step of the fluid dynamics (here, each frame shows the vorticity of the fluid). (b) If  $t < T_{in}$  (i.e., we do not have enough input frames requires as inputs), we use temporal-wise interpolation to create  $T_{in} - t$  pseudo-views to supplement necessary frames as inputs to the foundation model.

suppress or inhibit the production or activity of the activator.

$$\partial_t u = D_u \partial_{xx} u + D_u \partial_{yy} u + R_u, \quad \partial_t v = D_v \partial_{xx} v + D_v \partial_{yy} v + R_v. \quad (1)$$

$D_u, D_v$  are diffusion coefficients ( $D_u = 5 \times 10^{-3}, D_v = 1 \times 10^{-3}$  in PDEBench [61]). We consider the Fitzhugh-Nagumo type of Reaction-Diffusion equation, which describes how an action potential travels through a nerve membrane ( $k$  is set as  $5 \times 10^{-3}$ ):

$$R_u(u, v) = u - u^3 - k - v, \quad R_v(u, v) = u - v \quad (2)$$

**Incompressible Navier-Stokes.** The Navier-Stokes equations govern the dynamics of fluid flow and serve as fundamentals for fluid simulations. It considers both the mass conservation and the momentum of fluid parcels.

$$\frac{\partial \mathbf{u}}{\partial t} = -(\mathbf{u} \cdot \nabla) \mathbf{u} + \nu \nabla^2 \mathbf{u} - \frac{1}{\rho} \nabla p, \quad (3)$$

where  $\mathbf{u}$  is the velocity field,  $\nu$  is the dynamic viscosity ( $\nu = 0.01$  in PDEBench),  $\rho$  is the fluid density (which is constant in incompressible Navier-Stokes),  $p$  is the fluid pressure. We also have  $\nabla \cdot \mathbf{u} = 0$  due to the incompressibility.

**Compressible Navier-Stokes.** The compressible Navier-Stokes equations differ from the incompressible version by accounting for variations in density, pressure, and temperature. The equations include both the conservation of mass (the continuity equation) and conservation of energy, in addition to the momentum conservation equation in the incompressible version.

$$\text{Mass Conservation:} \quad \frac{\partial \rho}{\partial t} + \nabla \cdot (\rho \mathbf{u}) = 0 \quad (4)$$

$$\text{Momentum Conservation:} \quad \frac{\partial (\rho \mathbf{u})}{\partial t} + \nabla \cdot (\rho \mathbf{u} \otimes \mathbf{u}) = -\nabla p + \nabla \cdot \boldsymbol{\tau} \quad (5)$$

$$\text{Energy Conservation:} \quad \frac{\partial (\rho e_t)}{\partial t} + \nabla \cdot [(\rho e_t + p) \mathbf{u}] = \nabla \cdot (\mathbf{u} \cdot \boldsymbol{\tau}). \quad (6)$$

On top of Eq. 3:  $\boldsymbol{\tau}$  is the viscous stress tensor  $\boldsymbol{\tau} = (\zeta + \nu/3)(\nabla \cdot \mathbf{u})$ ;  $\nu, \zeta$  are the shear and bulk viscosity, respectively;  $e_t = e + \frac{1}{2} |\mathbf{u}|^2$  is the total energy (internal + kinetic),  $e = p/(\Gamma - 1)$  and  $\Gamma = 5/3$ . When we define  $M = |v|/c_s$  as the Mach number and  $c_s = \sqrt{\Gamma p/\rho}$  as the sound velocity, PDEBench includes two simulation settings:  $M = 1$  and  $M = 0.1$ .

**Shallow Water.** The Shallow Water equation is a simplified version of the original Navier-Stokes equation, in the context where the scale of horizontal length and velocity is much greater than the vertical scale, and also the pressure distribution is assumed to be hydrostatic. Typical examples are atmospheric and oceanic modeling. It is derived by integrating the

Navier-Stokes equation over the vertical coordinate from the bottom to the free surface ( $h$ ), incorporating the gravitational acceleration ( $g$ ), and replacing horizontal velocities with depth-averaged ones.

$$\frac{\partial h}{\partial t} + \nabla \cdot (h\bar{\mathbf{u}}) = 0, \quad \frac{\partial \bar{\mathbf{u}}}{\partial t} + (\bar{\mathbf{u}} \cdot \nabla)\bar{\mathbf{u}} = -g\nabla h \quad (7)$$

In our Shallow Water simulation, our primary interest is in the free surface dynamics ( $h$ ). This is because, in many practical applications, such as predicting the propagation of surface waves, tsunamis, or tides, the primary quantity of interest is the free surface elevation itself. The horizontal velocity may not be as crucial for these specific phenomena if the primary goal is to understand or predict wave heights, arrival times, or surface oscillations.

In PDEBench, the shallow water simulation considers a 2D radial dam break scenario. On a square domain  $\Omega = [-2.5, 2.5]^2$ , we initialize the water height as a circular bump in the center of the domain:

$$h(t=0, x, y) = \begin{cases} h_0, & \text{for } \sqrt{x^2 + y^2} < r \\ h_1, & \text{for } \sqrt{x^2 + y^2} \geq r \end{cases} \quad (8)$$

$h_0 \geq h_1$  and we fix  $h_1 = 1$ . In PDEBench,  $h_0 = 2$  and the radius  $r$  is sampled from a uniform distribution  $\mathcal{U}(0.3, 0.7)$ .

**Summary** We summarize detailed inputs and outputs in Table 10.

Table 10. Inputs and outputs for learning different PDEs. “incomp-NS”: incompressible Navier-Stokes. “CNS”: compressible NS. “RD”: Reaction-Diffusion. “SWE”: shallow water equation.

PDE Simulations	Input	Input Shape	Output
RD	Activator ( $u$ ), inhibitor ( $v$ )	$T \times C \times H \times W (T = 10, C = 2)$	Activator ( $u$ ), inhibitor ( $v$ ) at $T + 1$
incomp-NS	Velocity ( $v_x, v_y$ ), pressure ( $p$ )	$T \times C \times H \times W (T = 10, C = 3)$	Velocity ( $v_x, v_y$ ), pressure ( $p$ ) at $T + 1$
CNS	Velocity ( $v_x, v_y$ ), pressure ( $p$ ), density ( $\rho$ )	$T \times C \times H \times W (T = 10, C = 4)$	Velocity ( $v_x, v_y$ ), pressure ( $p$ ), density ( $\rho$ ) at $T + 1$
SWE	Height ( $h$ )	$T \times C \times H \times W (T = 10, C = 1)$	Height ( $h$ ) at $T + 1$

### 8.4.2. Pretraining Results

We show results of multiphysics pretraining in Table 11. Although results may not be directly comparable due to different training settings, our multiphysics pretraining achieves comparable performance with previous SciML foundation models.

Table 11. “CNS”: compressible Navier-Stokes. “incomp-NS”: incompressible Navier-Stokes. “SWE”: shallow water equation. “RD”: Reaction-Diffusion.

Model	#Parameters (M)	CNS	incomp-NS	SWE	RD
UNet [26]	25	0.313	-	0.0521	0.0971
FNO [26]	7	0.130	-	0.00912	0.0321
MPP-Ti [43]	7	0.0442	-	0.0066	0.0168
DPOT-Ti [26]	7	0.0285	-	0.0056	0.0321
Ours	6.5	0.195	0.094	0.0056	0.0621